Effect of Cu Content on Corrosion Behavior of 7xxx Series Aluminum Alloys

Qingjiang Meng* and G. S. Frankel**

Fontana Corrosion Center, Department of Materials Science and Engineering, The Ohio State University,

The corrosion behavior of 7xxx aluminum alloys with various Cu content was investigated using polarization and electrochemical impedance spectroscopy (EIS) techniques. Two breakdown potentials were found in Cu-containing alloys in deaerated chloride solution, and the values increased logarithmically with increasing Cu content. However, in aerated chloride solution, polarization resistance as determined by EIS decreased with increasing Cu content. The first breakdown potential corresponded to transient dissolution associated with attack of the fine hardening particles and the surrounding solid solution in a thin surface layer. The second breakdown potential was associated with combined intergranular and selective grain attack. The correlation between the microstructure, especially Cu content, and corrosion behavior was made by composition analysis of the grain boundary regions including precipitate free zone and grain boundary precipitates as well as the matrix by scanning transmission electron microscopy. The corrosion potential increased with increasing alloy Cu content in aerated chloride solutions because of enhanced rates of oxygen reduction. This degraded the corrosion resistance despite the increase in the breakdown potentials with Cu content.

High strength Al alloys such as AA7075 and AA7178 are commonly used in aircraft structure applications. The addition of Cu as one of alloying elements in Al-Zn-Mg alloys greatly improves the mechanical strength of 7xxx series alloys (AA7xxx) by precipitation hardening. The peak aged T6 temper provides the maximum mechanical strength. However, Cu-containing AA7xxx alloys in the T6 temper (AA7xxx-T6) are susceptible to various forms of localized corrosion in chloride environments, such as pitting, crevice, intergranular corrosion (IGC), and exfoliation corrosion. As pits or crevices grow, they often develop into IGC, which can propagate rapidly and deeply into a structure. In addition, Cu enrichment and redistribution, which arise from dealloying of Cu-rich intermetallics and the matrix, have been observed in Cu-containing Al alloys in chloride solution and further accelerate the corrosion process.[1-3]

The microstructure of AA7xxx-T6 is heterogeneous, containing the Al matrix, coarse intermetallic compound particles (IMCs), and the grain boundary region, including the precipitate free zone (PFZ) and grain boundary precipitates. Cu is distributed in the microstructure of AA7xxx-T6 in different forms. In the Al matrix, fine hardening precipitates on the order of nanometers in size, such as Guinier-Preston (GP) zones or η' phase, contain most of the Cu in the alloy.[4] Cu also exists in coarse IMCs of about a few micrometers in size, such as Al_2CuMg (S), Al_2Cu (θ), or Al_7Cu_2Fe particles, and in the grain boundary precipitates of about 50-100 nm size, such as Mg $(ZnCuAl)_2$.[4-7]

The Cu distribution in the microstructure affects the susceptibility to localized corrosion. Pitting corrosion usually occurs in the Al matrix near Cu- or Fe-containing intermetallic particles

owing to galvanic interaction with the Al matrix.[8] IGC is generally believed to be associated with Cu-containing grain boundary precipitates and the PFZ along grain boundaries.[4,9] The grain boundary regions in AA7075-T6 and AA7150-T6 have been investigated using analytical transmission electron microscopy.[9-11] The PFZ was about 30-70 nm on either side of the boundaries and the grain boundary precipitates were about 50-100 nm in size. Zn and Cu depletion were found in the PZF in both alloys. On the grain boundaries in AA7150, $MgZn_2$ precipitates with considerable solubility of Cu and Al were identified. The Cu content in the precipitates was about 12 atom %. It is difficult to quantitatively measure the exact composition of the PFZ and grain boundary precipitates due to experimental limitations, such as the relatively large electron probe size in analytical transmission electron microscopy, the narrow PFZ regions, and the small size of the precipitates on grain boundaries.

Electrochemical measurements have been conducted on AA7xxx, especially AA7075 and AA7150 in the T6 temper in de-aerated NaCl solution.[9,12] Two breakdown potentials have been found in potentiodynamic polarization scans. Maitra and English[12] suggested that for AA7075-T6, the active breakdown potential was associated with IGC and the noble breakdown potential with pitting in the matrix. They attributed the IGC susceptibility of the T6 temper to Mg and Zn solute segregation or enrichment in the grain boundary regions. It was suggested that this enrichment caused the grain boundary region to have a more active breakdown potential than the matrix. However, this inference was contradicted by Park and Ardell, who used analytical transmission electron microscopy (TEM) to show that the grain boundary region in AA7075-T6 exhibited considerable Zn depletion relative to the matrix. Ramgopal *et al.* characterized the grain boundary region in AA7150-T6 using analytical TEM and thin-film analogs of the PFZ and grain boundary precipitates.[9,13] The open-circuit potential (OCP) and breakdown potential for grain boundary $Mg(ZnCuAl)_2$ precipitates in deaerated 0.5 M NaCl increased with Cu content. Based on artificial crevice polarization experiments, it was proposed that IGC in the T6 temper was caused by anodic dissolution of $Mg(ZnCuAl)_2$ grain boundary precipitates, which led to the creation of aggressive occluded environments. This anodic dissolution mechanism for IGC was also found in Al-Li-Cu alloys.[14-16]

Most investigations reported in the literature have focused on high Cu content Al alloys such as AA7075 and AA7150. The relationship between the microstructure, especially Cu content, and corrosion behavior is still unclear. To investigate the role of Cu content, the corrosion behavior of several AA7xxx-T6 alloys, with Cu content ranging from essentially Cu-free up to 2 wt %, in deaerated and aerated NaCl solution was studied in this work. Metallography and focused ion beam (FIB) sectioning of the corroded alloys were employed to determine the corrosion forms. The grain boundary regions were characterized using state-of-the-art scanning TEM (STEM), which provided a better understanding of the correlation between the microstructure and corrosion behavior of AA7xxx-T6.

Experimental

Five types of AA7xxx in the T6 temper with various Cu contents were used in this work. The compositions of these alloys, as determined by inductively coupled plasma mass spectroscopy (ICP-MS), are listed in Table I. The AA7004 alloy contains only 0.013 wt % Cu and can be considered to be essentially Cu-free. AA7039, AA7075, and AA7050 were

Table I. Composition of 7xxx Al alloys measured by ICP-MS in wt %.

Alloy	Zn	Mg	Cu	Cr	Fe	Si	Mn	Al
7004	4.3	1.6	0.013	⋯	0.09	0.02	⋯	Bal
7039	4.0	2.9	0.077	0.19	0.17	0.05	0.26	Bal
7029	4.6	1.7	0.69	⋯	0.08	0.02	⋯	Bal
7075	5.4	2.4	1.36	0.18	0.24	0.04	0.03	Bal
7050	5.9	2.0	2.0	0.01	0.09	0.03	0.01	Bal

commercial grade sheets purchased in the T6 temper. AA7004 and AA7039 were not commercially available, so they were cast by vacuum induction melting, homogenized at 500°C for 6 h, and hot-rolled to sheets. The rolled sheets were solution heat treated at 475°C for 30 min and quenched in water, then artificially aged at 120°C for 24 h to create the T6 temper. Samples were cut from these five alloy sheets. A nonaqueous polishing procedure was used to minimize corrosion during polishing. The samples were mechanically ground to 1200 grit finish with ethanol, cleaned ultrasonically in ethanol, and finally dried by a cold air stream.

Microhardness measurements on the five types of Al alloys were conducted using a Buehler Micromet II digital microhardness tester. The load to make a pyramid indentation was 300 g and the load time was 20 s.

The microstructures of the Al alloys were characterized using optical metallography, scanning electron microscopy (SEM), TEM, and STEM. Optical metallography was performed on samples with three different orientations (L, LT, and ST) that were polished to 1 µm finish with alumina suspended in ethanol followed by etching in Keller's reagent for about 30 to 60 s. SEM characterization was performed on corroded samples using an FEI Sirion SEM with a field-emission gun (FEG-SEM) operating at 12 kV. TEM characterization was performed using a Philips CM200T TEM operating at 200 kV.

TEM samples of the alloys were prepared by an FEI Strata dual beam 235M FIB using a 30 keV Ga ion beam and 5 keV electron beam. The samples had an area of about 15 × 5 µm and were thinned in the FIB to about 100 nm for electron transparency. The samples were then plucked out of the bulk under an optical microscope using a sharp Pyrex needle of about 1 µm diameter, and placed on a 200 mesh Au specimen grid with a Formvar/carbon support film for TEM and STEM analysis.

STEM characterization of the grain boundary precipitates and PFZ was conducted with an FEI Tecnai TF20 STEM operating at 200 kV. The drift-corrected energy-dispersive spectroscopy (EDS) line profiles were acquired and quantified using the FEI/Emispec TIA software. The probe size was less than 2 nm with sufficient brightness supplied by an FEG and the step size was about 5 nm. The dwell time for each pixel point was 5 s. The EDS quantification used the Cliff-Lorimer method with theoretical k factors.[17]
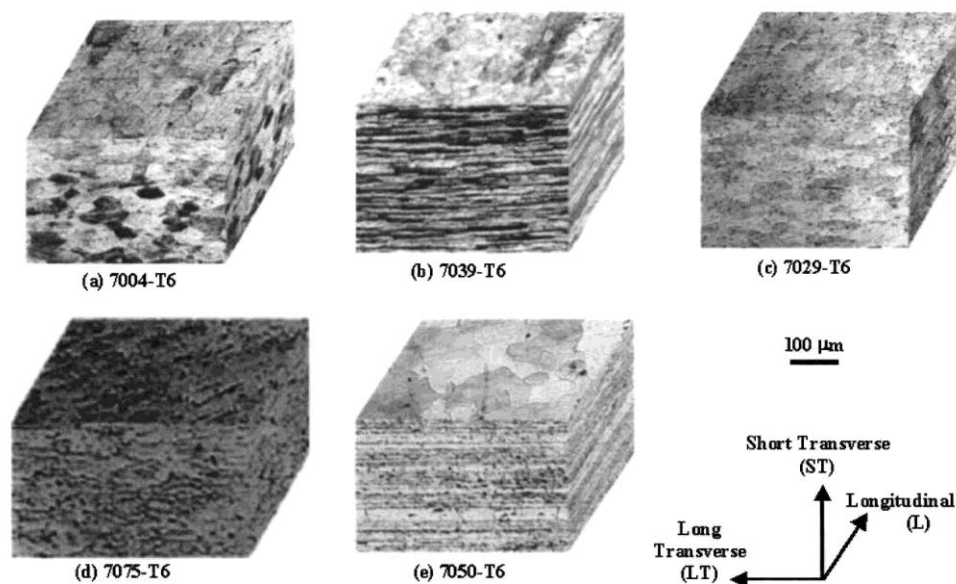
Figure 1. Microstructure of three orthogonal sections of (a) AA7004-T6, (b) AA7039-T6, (c) AA7029-T6, (d) AA7075-T6, and (e) AA7050-T6 sheets.

Table II. Coarse intermetallic particles identified by SEM/EDS

Alloy	Coarse intermetallics
7004	Al_3Fe
7039	$Al_3(FeSi)$
7029	$Al_3(FeCuSi)$
7075	Al_2CuMg, $Al_3(FeCu)$, Mg_2Si
7050	Al_7Cu_2Fe

Electrochemical polarization measurements were performed on samples ground to 1200 grit. The pH of the 0.5 M NaCl solution was adjusted to 3.56 by the addition of HCl. The solution was deaerated with Ar gas to decrease the corrosion potential and allow for clear observation of the breakdown potentials. Potentiodynamic scans were performed at a rate of 0.2 mV/s. Potentiostatic polarization tests were conducted at different potentials relative to the breakdown potentials for 1, 5, and 24 h. Polarization experiments were performed using a Gamry PC4/FAS1 potentiostat. A Pt counter electrode and saturated calomel reference electrode (SCE) were used. All potentials in this paper are referenced *vs.* SCE. The corrosion morphologies of the surfaces and cross sections were examined metallographically after polarization tests to determine the nature of attack.

To ensure the validity of the metallography, same samples were cross sectioned after potentiostatic polarization tests with FIB. Rough sectioning was performed first with the ion beam perpendicular to the corroded surface at a current of 20 nA. Final fine sectioning was performed at a current of 1 nA. The sample was then tilted to 30° to conduct SEM imaging of the cross section in the crater.

To study the change in composition of the sample surface after the polarization tests, X-ray photoelectron spectrometry (XPS) measurements were performed using an AXIS Ultra

spectrometer controlled by a VISION data system. The entrance and exit slit widths for the hemispherical analyzer were set to 4 mm and a pass energy of 20 eV was used. A monochromatic Al Kα X-ray line with energy of 1486.6 eV and 150 W was used as the incident radiation source. The take-off angle was 90°. The binding energies (BEs) of the elements of interest were calibrated with respect to the C 1s line at 284.5 eV.

Electrochemical impedance spectroscopy (EIS) measurements were performed at the OCP during 168 h immersion of the samples in 0.5 M NaCl open to the air. The impedance measurements were performed as a function of frequency between 10 kHz and 10 mHz using a sinusoidal voltage modulation of 10 mV. The experiments were conducted using a Princeton Applied Research (PAR) model 273 potentiostat with a Solartron model 1255 frequency-response analyzer. The OCP during the immersion was also recorded. The polarization resistance was determined using a Kramers-Kronig transform.[18] The values determined in this fashion were very close to those determined by fitting the data to a simple Randles equivalent circuit.

Results

Microstructure.—Figure 1 shows orthogonal metallographic microstructures for the five AA7xxx-T6 sheets. All alloys have an elongated grain structure even though the aspect ratios are different. SEM/EDS was used to identify the coarse intermetallic particles. The type and composition of the coarse intermetallic particles are listed in Table II. Figure 2 shows the microhardness data for the five AA7xxx alloys. The hardness increased with increasing Cu content, which supports the notion that the addition of Cu into Al-Zn-Mg alloys improves the mechanical strength of AA7xxx by precipitation hardening.

TEM and STEM were used to characterize the microstructure of all alloys on a microscopic scale. Figure 3 shows TEM bright-field micrographs of the grain boundary regions of all five alloys. Fine hardening precipitates are evident in the matrix. PFZ and grain boundary precipitates are found in each alloy. The compositions of the matrix, PFZ, and grain boundary precipitates were determined by STEM/Nano-EDS. The composition of the matrix including the hardening precipitates, which mirror the composition of the precipitates on the grain boundary, was very close to the nominal alloy composition for each alloy. The composition of the PFZ was almost identical for all five alloys: Al containing about 2 wt % Mg with little of the other alloying elements. The measured composition of the grain boundary precipitates deviated considerably from the expected stoichiometry of $Mg(ZnCuAl)_2$. This deviation occurred because the small grain boundary precipitates did not extend through the whole thickness of the TEM foils, which were about 100 nm thick. As a result, the X-ray excitation volume included both the precipitates and the surrounding Al-rich PFZ, and the measured Al concentration in the precipitates was erroneously high. To correct for this artifact and determine the exact composition of the grain boundary precipitates, the approach of Ramgopal *et al.* was followed. The composition of the PFZ was assumed to be Al-2% Mg and the PFZ was considered to be the only material in the X-ray excitation volume when the probe was positioned in the center of the PFZ. It was further assumed that the stoichiometry of grain boundary precipitates was $Mg(ZnCuAl)_2$ since η phase has considerable solubility for Cu and Al.[4] The Mg concentration in this Cu-and Al-containing η phase was fixed at 33.33 atom % regardless of the Cu and Al concentration. Based on these assumptions, the measured composition of the precipitate, $(C_i)_{mp}$, is a sum of contribution from the PFZ and the precipitates[9]

$$(C_i)_{mp} = V_{pfz}(C_i)_{pfz} + V_p(C_i)_p \qquad\qquad [1]$$

where C_i is the composition of the ith element (Mg,Zn,Cu,Al) in atom %; $(C_i)_{mp}$ is the measured composition of the precipitate in atom %; $(Ci)_{pfz}$ is the composition of the PFZ, which is considered be Al-2 wt % Mg (2.2 atom % Mg); $(C_i)_p$ is the calculated actual composition of the precipitate in atom %; V_{pfz} and V_p are the fractions of the X-ray excitation volume for the PFZ
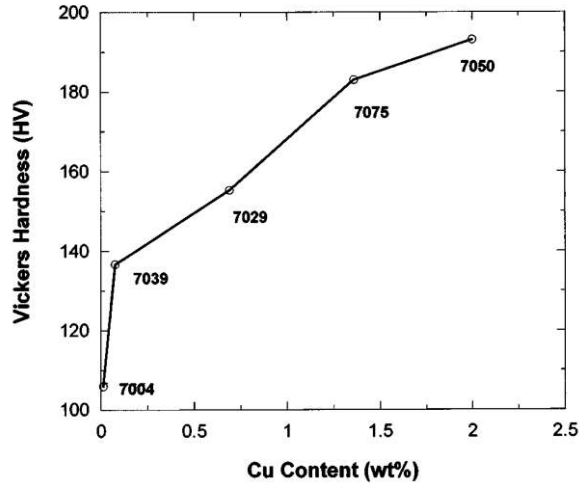

Figure 2. Microhardness *vs.* Cu content curve showing that Cu addition increases the hardness of AA7xxx-T6.
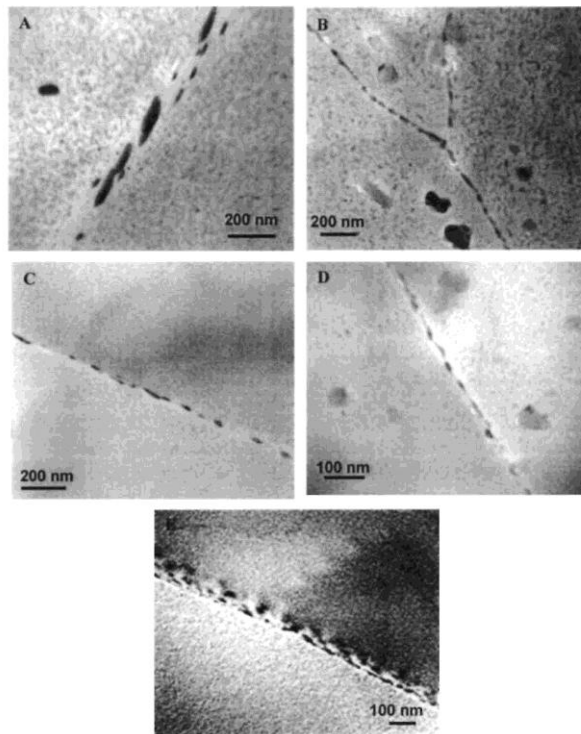

Figure 3. TEM micrographs showing the grain boundary regions in (a) 7004, (b) 7039, (c) 7029, (d) 7075, and (e) 7050 alloys.
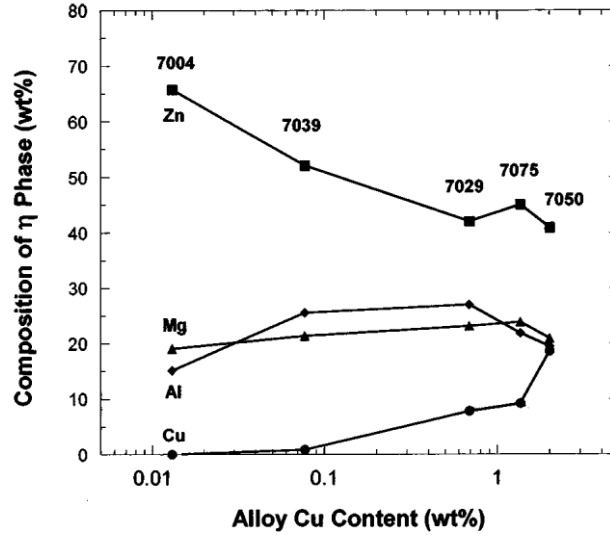
Figure 4. Composition of η phase precipitates on grain boundary as a function of alloy Cu content in AA7xxx-T6.

and precipitate, respectively, during analysis of the precipitate. The volume fractions were determined from the Mg analysis and by fixing the Mg content in the precipitate at 33.33 atom %. Because the probe and X-ray excitation volume were much smaller than the precipitates, the accuracy for composition calculation mostly depended upon the accuracy for EDS quantification. The EDS quantification was made using the Cliff-Lorimer method with theoretical k factors. Figure 4 shows the calculated composition of η phases in the five AA7xxx alloys converted to wt %. The Mg concentration was fixed at 33.33 atom %, but the wt % varied slightly as the composition of the particles changed for each alloy. The Al concentration in the grain boundary precipitate also remained nearly at the same level for the five alloys. However, with increasing alloy Cu content, the Cu concentration in the precipitate dramatically increased from zero in AA7004 up to 18.6 wt % in AA7050, and the Zn concentration in the precipitate decreased from 65.8 wt % in AA7004 down to 41.0 wt % in AA7050.

Table III. Breakdown potentials for AA7xxx-T6 in deaerated 0.5 M NaCl at pH 3.56.

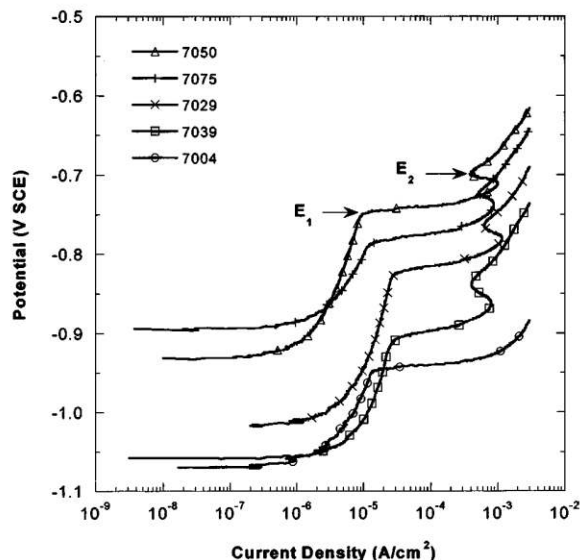| Alloy	E_1 (mV$_{SCE}$)	E_2 (mV$_{SCE}$)	$E_2 - E_1$ (mV)
7004	N/A	-951 ± 3	N/A
7039	-905 ± 4	-835 ± 6	70
7029	-821 ± 3	-766 ± 1	55
7075	-780 ± 4	-720 ± 2	60
7050	-751 ± 3	-699 ± 1	52

Figure 5. Potentiodynamic polarization curves for AA7xxx-T6 in deaerated 0.5 M NaCl at pH 3.56 with a scan rate of 0.2 mV/s.

Polarization curves and types of corrosion.—Figure 5 shows the anodic polarization curves for AA7xxx-T6 alloys with various Cu contents in deaerated 0.5 M NaCl solution with pH 3.56. Two breakdown potentials were found for all except the Cu-free AA7004. The data for the breakdown potentials are listed in Table III. For the alloys exhibiting two breakdown potentials, a sharp increase in current density occurred at the lower, more active breakdown potential referred to as the first breakdown potential (E_1). As the potential increased further, the current density increased until it reached a value of about 1 mA/cm , and then decreased. Above the more-noble breakdown potential, referred to as the second breakdown potential (E_2), the current increased again. This indicates that the dissolution between E_1 and E_2 was not stable, and stable dissolution occurred only above E_2. Two breakdown potentials for Cu-containing AA7xxx-T6 have been reported in the literature.[9,12] Figure 6 shows the relationship between the breakdown potentials and alloy Cu content on a semi-logarithmic scale. For the Cu-containing alloys, both breakdown potentials increased logarithmically with increasing Cu content. The difference between the two breakdown potentials for Cu-containing alloys was nearly constant, 52-70 mV, as shown in Table II and Fig. 6. For Cu-free AA7004, only the second breakdown potential was observed, and it was associated with stable dissolution. Extrapolation of the line fitting the E_1 values to the Cu content of AA7004 indicates that an expected E_1 value for this alloy, if it exists, would be about —985 mV$_{SCE}$. This is discussed in more detail below.

To determine the types of attack corresponding to each breakdown potential, constant-potential tests were conducted at different potentials relative to the breakdown potentials in the same deaerated NaCl solution. All Cu-containing alloys exhibited similar potentiostatic polarization behavior. Figure 7 shows the current density transients for AA7075-T6 at various applied potentials from just above the first breakdown potential to well above the second breakdown potential (E_1 = — 780 mV$_{SCE}$ and $E2$ = —720 mV$_{SCE}$). The current
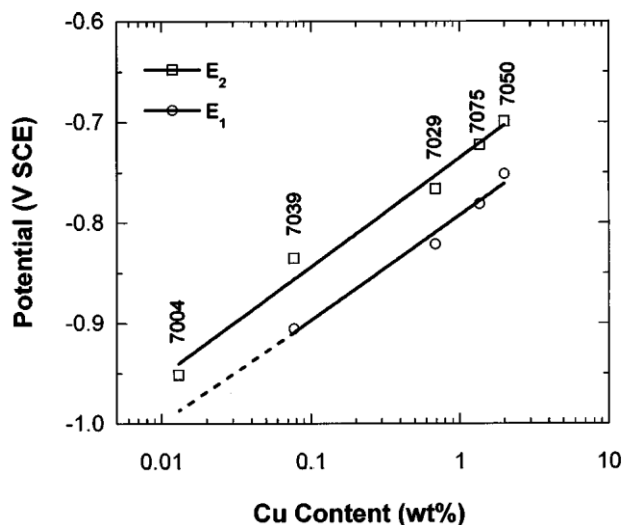
Figure 6. Correlation between the breakdown potentials in deaerated 0.5 M NaCl at pH 3.56 and the alloy Cu content.
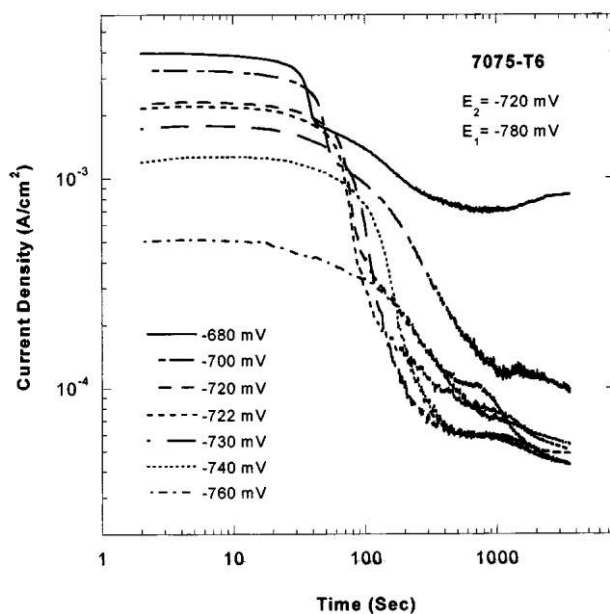

Figure 7. Current transients at various applied potentials for AA7075-T6 in deaerated 0.5 M NaCl at pH 3.56.

densities were on the order of 1 mA/cm^2 within the first tens of seconds during polarization then decreased dramatically. At applied potentials between E_1 and E_2, the current densities decreased to about 3×10^{-5} A/cm^2 after 1 h, which was close to the value of passive current density in the pH 3.56 solution. Above E_2, the current densities at 1 h were much higher, 1×10^{-4} and 8×10^{-4} A/cm for potentials of —700 and —680 mV$_{SCE}$, respectively.

The charge densities for the Cu-containing alloys during the 1 h potentiostatic polarization were calculated by integration of the current density. Figure 8 shows the variation of

charge density as a function of applied potential for all five alloys. Cu-free AA7004 with only one breakdown potential behaved differently than the other four Cu-containing alloys with two breakdown potentials. For AA7004, the charge density increased dramatically above the single breakdown potential. For the Cu-containing alloys, the charge densities were very small (about 0.45 C/cm^2) for potentials between E_1 and E_2. These small amounts of charges were mostly generated by the large current transient occurring at the very beginning of polarization. However, when the applied potential was above E_2, the charge density increased dramatically with further increasing applied potential. Therefore, the first breakdown potential E_1 was due mostly to transient dissolution on the surface. In contrast, stable or sustained dissolution occurred above the second breakdown potential E_2.
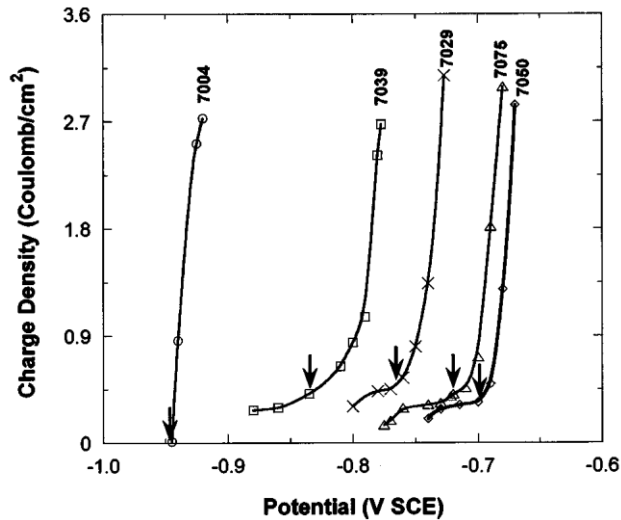

Figure 8. Variation of charge density as a function of applied potential in 1 h potentiostatic polarization for AA7xxx-T6 in deaerated 0.5 M NaCl at pH 3.56. The arrows show the values of E_2 for each alloy.

To further determine the corrosion forms corresponding to transient dissolution and sustained dissolution at E_1 and E_2, respectively, the corrosion morphology was examined after potentiodynamic and potentiostat polarization tests. Figure 9 shows the surface morphologies of all five alloys, which were potentiodynamically polarized to the current density of 1 mA/cm^2. The final potential for each scan was between the two breakdown potentials for each alloy except for AA7004, where the final potential was higher than the single breakdown potential. Again, the behavior of AA7004 was different than that of the other alloys. Many pits were found on the surface of AA7004 after this treatment. In contrast, large dark corroded regions without obvious pits and some bright uncorroded regions were found on the originally shiny surface of the Cu-containing alloys. This dark corrosion morphology is discussed in more detail below.

Since the Cu-containing alloys have similar polarization behavior, AA7075-T6 with intermediate Cu content was studied in more detail in this work. An AA7075-T6 sample was cyclically polarized in deaerated 0.5 M NaCl three times, Fig. 10. The apex current densities for the three scans were 3, 10, and 10 mA/cm^2, respectively. When each cycle was finished, the sample was left at open circuit until the OCP of the sample was stable. As shown in Fig. 10, two

breakdown potentials ($E_1 = $ —780 mV$_{SCE}$ and $E_2 = $ —720 mV$_{SCE}$) were evident in the first cycle. In the second and third cycles, the first breakdown in the first scan disappeared and only the second breakdown was seen. The sample surface changed during the exposure at potentials between E_1 and E_2 as a result of the transient attack. In contrast, the second breakdown potential was reproducible in subsequent cyclic polarization and corresponds to stable forms of dissolution such as pitting and IGC.

To further identify the cause of transient dissolution between the two breakdown potentials, another AA7075 sample was polarized at —725 mV$_{SCE}$, which is between the two breakdown potentials, for 500 s in deaerated 0.5 MNaCl, pH 3.56. Figure 11 shows a current transient similar to the curves shown in Fig. 7, except that there is a short period of increasing current at the start. The current density was high at the beginning (about 10^{-3} A/cm^2) and then decayed to 4×10^{-5} A/cm after about 300 s. The total charge during 500 s for 1 cm^2 exposure area of the sample was calculated to be 0.217 C. During polarization, it was observed by the unaided eye that several dark spots appeared and spread out on the originally shiny sample surface until the whole surface became dark. After the polarization test, the sample was rinsed gently with deionized (DI) water and dried rapidly in a desiccator. Nearly the whole surface was dark under an optical microscope, similar to the corrosion morphology shown in Fig. 9d. Figure 12 shows secondary and backscattered electron images of the sample. The dark region observed by the unaided eye and the optical microscope was a thin layer, which seemed to undergo uniform corrosion and could be corrosion product uniformly covering the surface. This thin layer is rippled, a feature probably caused during rinsing with DI water. Also shown in Fig. 12 is a region at the middle of the SEM images that was an uncorroded residual surface region.

Because this thin uniformly corroded layer on the surface is estimated to be much less than 1 µm based on the SEM images as shown in Fig. 12, SEM/EDS is not suitable to measure its composition. XPS was performed on this treated AA7075 sample and on an as-polished sample surface for composition comparison. On the as-polished sample surface, the naturally formed Al oxide was a few nanometers thick,[4] which was less than the analysis depth for pho-

(a) 7004   (b) 7039   (c) 7029
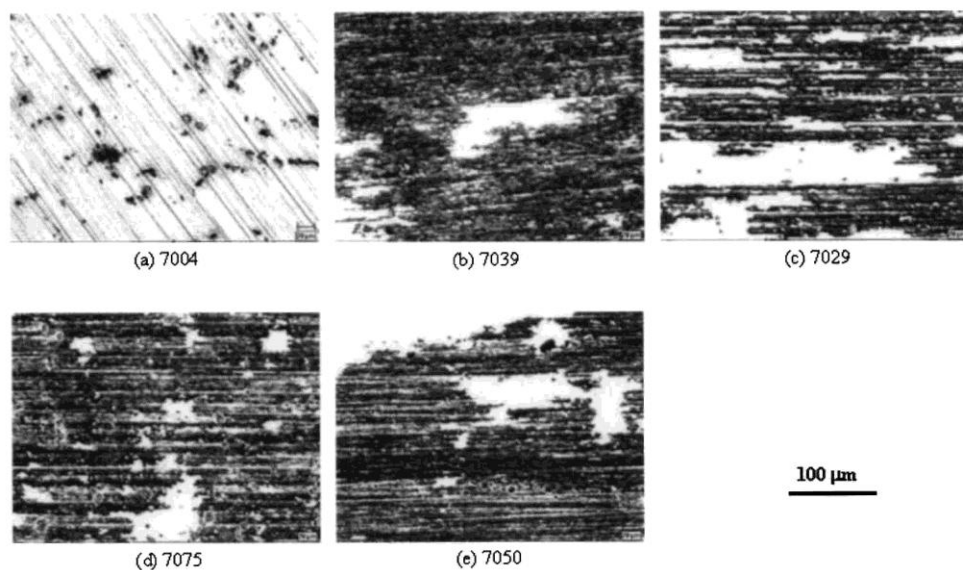
(d) 7075   (e) 7050

100 µm

Figure 9. Optical micrographs of (a) 7004, (b) 7039, (c) 7029, (d) 7075, and (e) 7050 samples potentiodynamically polarized to the current density of 1 mA/cm^2 in deaerated 0.5 M NaCl at pH 3.56.

toelectrons with a take-off angle of 90°.[19] Hence, the photoelectrons in the XPS measurements originated from both the Al oxide and underlying Al matrix in the as-polished sample. In the polarized sample, the photoelectrons were produced mainly from the thin corroded layer or corrosion product. Figure 13 shows XPS spectra for Al, Zn, Mg, Cu, O, and Cl. The C 1s spectra for the as-polished and polarized samples were also obtained for energy calibration. The detailed data obtained from the XPS spectra are listed in Table IV. The oxidation states were determined using the XPS database.[19] The BE for the elements in the Al matrix deviated from the BE for the standard pure metals. The comparison of XPS spectra for the as-polished and polarized samples in Fig. 13 provides important clues regarding the surface change after the polarization between the two breakdown potentials. Al^0 in the matrix was visible in the Al 2p spectrum for the as-polished sample, but not for the polarized sample. The Al and O spectra indicate the
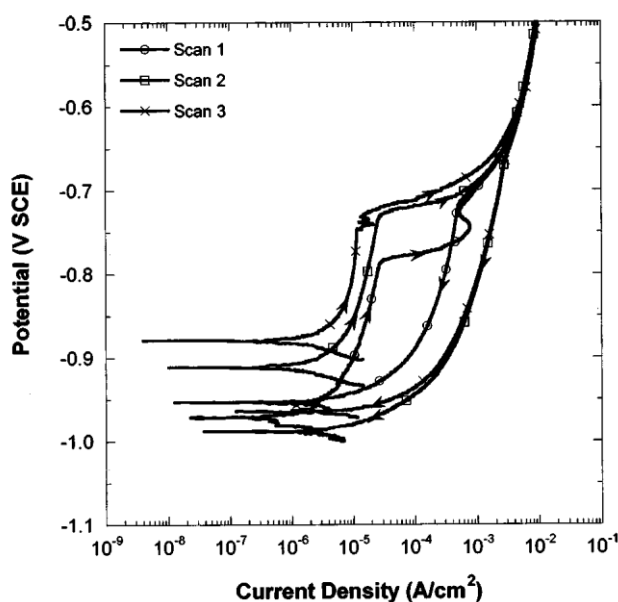

Figure 10. Cyclic anodic polarization curves for the same AA7075-T6 sample in deaerated 0.5 M NaCl at pH 3.56 at a scan rate of 0.2 mV/s. The sample was polarized three times: the apex current densities for three scans were 3, 10, and 10 mA/cm², respectively. When each cycle was finished, the sample was left at open circuit until the OCP was stable.

formation of $Al(OH)_3$ on the polarized sample surface. In addition, Mg disappeared and the amount of Zn was reduced, while Cu was enriched on the polarized sample surface. Chloride was also found on the polarized sample surface, as expected. The change in chemical states and amounts of the elements indicates that preferential dissolution of Mg, Al, and Zn occurred during the polarization between the two breakdown potentials, in a fashion similar to dealloying of Cu-containing intermetallic particles like Al_2CuMg.

A cross-sectional foil of the surface of this treated AA7075 sample was prepared by FIB and examined by TEM. Figure 14 shows the product layer and underlying Al substrate in cross-sectional view. The $Al(OH)_3$ layer was about 120 nm thick and the selected area diffraction pattern indicated that it was amorphous. The roughness of the interface between the layer and Al matrix suggests that the product layer was produced by uniform attack of the Al matrix.
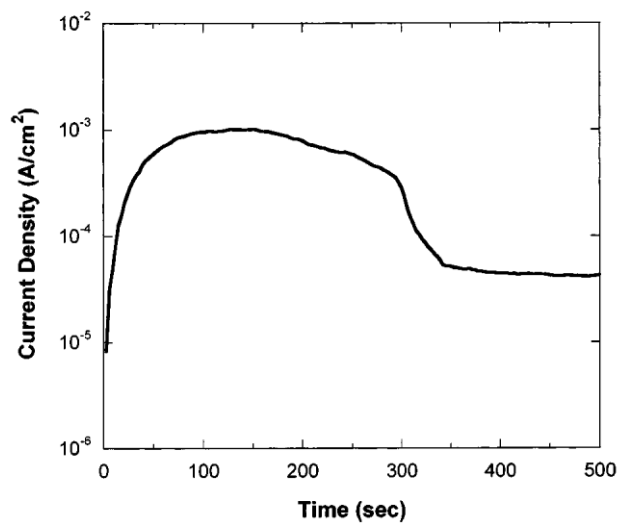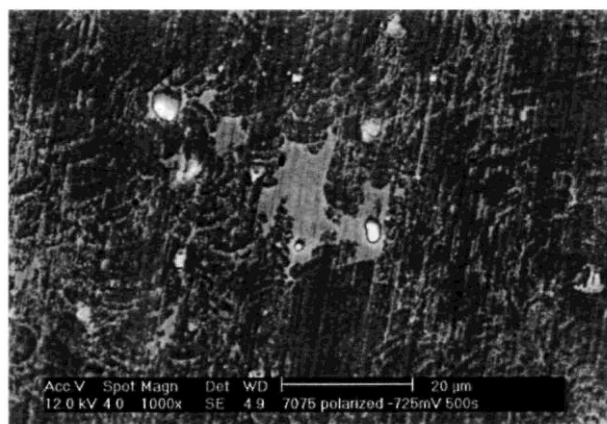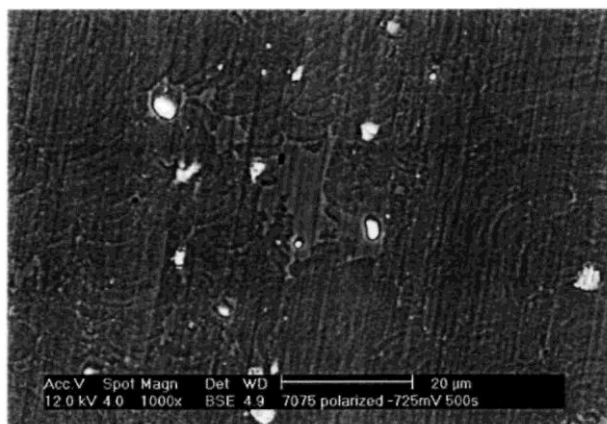
Figure 11. Current transient of AA7075 polarized at —725 mV$_{SCE}$ for 500 s in deaerated 0.5 M NaCl at pH 3.56.

Figure 12. SEM (a) secondary electron and (b) backscattered electron images of the surface of AA7075 sample polarized at —725 mV$_{SCE}$ for 500 s in deaerated 0.5 M NaCl at pH 3.56.

The potentiodynamic polarization experiments described above were relatively short in duration. The corrosion morphology was also examined after long-term potentiostatic polarization tests. AA7039-T6 and AA7050-T6 samples representing low and high Cu content,

respectively, were polarized at potentials between their two breakdown potentials in deaerated 0.5 M NaCl, pH 3.56 for 24 h. The potentials applied to AA7039 and AA7050 were —870 and —720 mV$_{SCE}$, respectively. Similar to the curves in Fig. 7, one large current transient was observed at the beginning of these two long-term polarization tests, followed by a low current density on the order of 10^{-5} A/cm^2. Figure 15 shows the corrosion morphologies of AA7039 and AA7050 after the 24 h polarization tests. Small pits and semi-continuous shallow attack were found on the grain boundaries in the low Cu content AA7039. The high Cu AA7050 exhibited continuous and relatively deep IGC attack as well as corrosion product on the attacked grain boundaries. These morphologies indicate that IGC attack occurred in both alloys during 24 h exposure between E_1 and E_2.

An AA7075-T6 sample was polarized at —680 mV$_{SCE}$ in deaerated 0.5 M NaCl, pH 3.56 for 5 h. This potential is above the second breakdown potential of AA7075 (E_2 = —720 mV$_{SCE}$). Figure 16 shows the corrosion morphology of AA7075 in top view and metallographic cross-sectioned view. The corrosion morphology in AA7075 reveals a combination of IGC and selective grain attack, sometimes referred to as microstructural pitting.[20] To ensure that the metallographic corrosion morphology is not an artifact due to grain fallout during mechanical polishing, the same AA7075 sample was cross sectioned after polarization using FIB. It is evident in Fig. 17 that the FIB section also reveals a combination of IGC and selective grain attack. This mode of attack involves complete dissolution of certain grains. The attack ceases at the neighboring grain, instead of continuing to form a typical hemispherical isotropic pit. Intergranular attack can be seen at the neighboring grain face and in the underlying region in the FIB-etched section.

EIS measurement under free corrosion conditions.—All previous electrochemical polarization measurements were performed in deaerated NaCl solution and were controlled by a potentiostat, which can supply as much current as is needed to support anodic dissolution of the alloys. In reality, corrosion occurs under free corrosion conditions, where local cathodes on the surface supply cathodic current to support anodic reactions at the local anodes. The primary cathodic reaction to consider in aerated neutral solutions is oxygen reduction. To investigate this type of exposure, all five alloys were immersed in stagnant, air exposed 0.5 M NaCl solution for up to 168 h. Figure 18 shows the OCP as a function of immersion time. The OCP increased with Cu content in the alloys. The OCPs for Cu-free AA7004 and AA7039, which has only 0.077 wt % Cu, decreased after 48 h immersion, eventually reaching low values. In contrast, the OCP for the intermediate and high Cu-containing alloys remained constant, at values about equal to their respective E_2 potentials. EIS measurements were carried out at OCP during this immersion time. Figure 19 shows the variation of low frequency impedance or polarization resistance for all five alloys as a function of immersion time. The polarization resistance of high Cu-containing alloys was lower than that for low Cu-containing alloys under free corrosion conditions. It is known that Cu enrichment and redistribution occur in Al-Cu and Al-Cu-Mg alloys as a result of dealloying of the Cu-containing matrix and active Cu-containing intermetallic inclusions such as Al$_2$CuMg particles.[1–3,21–25] Cu particles can be released, corrode, and then redeposit back on the surface. Cu enrichment and redistribution in Al-Zn-Mg-Cu alloys during free corrosion could

account for the variation of OCP and polarization resistance as a function of immersion time. For high-Cu alloys such as AA7075 and AA7050, Cu remnants or clusters develop with time. These Cu-rich areas on the surface are cathodic sites that facilitate oxygen reduction, which drives the corrosion process. For these alloys, the OCP remains high and the corrosion rate (inversely related to the polarization resistance) increases with time. For AA7004 and AA7039, Cu enrichment and redistribution are negligible or less significant. Without Cu enrichment, there is insufficient cathodic reaction to sustain localized corrosion. As a result, the OCP drops, and the corrosion rate remains low and decreases with time in Al-Zn-Mg alloys.

Discussion

Mechanism of localized corrosion of AA7xxx-T6.—To develop a better understanding of the role of Cu content in corrosion behavior, it is necessary to understand the mechanism of localized corrosion of AA7xxx-T6. It is generally recognized that there should be a relationship between corrosion behavior and alloy composition and microstructure. By studying corrosion behavior and microstructure of a series of AA7xxx with various Cu content, it is possible to establish this relationship.

One key observation from the polarization curves described above is that all alloys have almost the same difference between their two breakdown potentials, about 50-70 mV. This implies that the two types of dissolution or corrosion corresponding to the two breakdown potentials are related to each other, although the first breakdown potential corresponds to transient dissolution, while stable dissolution occurs above the second breakdown potential.

Both potentiostatic polarization between the two breakdown potentials and potentiodynamic polarization to 1 mA/cm^2 with the final potential between the two breakdown potentials led to the creation of dark corroded regions on the surface. The morphology of the dark regions observed using SEM indicates it is a corrosion product. Since the applied potentials were still below the second breakdown potentials, no large and deep pits were observed on the surface. This excludes the possibility that the corrosion product was produced from large discrete pits and deposited on the un-attacked surface. XPS surface analysis proves that the dark regions are attacked uniformly and the thin surface layer is mainly Al(OH)$_3$ with Cu enriched and Mg depleted. TEM observation on the FIB prepared cross section of the layer and underlying Al matrix further proves that the Al matrix surface was subject to corrosion attack and the amorphous hydroxide layer was produced by direct attack of the Al matrix.

This uniform corrosion on the surface could be attributed to dealloying of fine hardening precipitates containing Cu. Electrochemical studies revealed that Cu-containing intermetallic particles such as Al$_2$CuMg and Mg(ZnAlCu)$_2$ are susceptible to dealloying in chloride solution.[13,26] These Cu-containing intermetallics exhibit their own breakdown potentials for dealloying.[13,26]

After the polarization of AA7075 at —725 mV$_{SCE}$ for 500 s, the charge for 1 cm exposure area was 0.217 C. Assuming a uniform dissolution process that was 100% current efficient, simplifying the Al matrix (91% Al) as 100% Al, and applying Faraday's law, the depth of Al matrix dissolved can be determined to be 75 nm. This calculated value is on the same order of magnitude as the 120 nm thick uniform Al(OH)$_3$ layer observed by TEM. This further supports the notion that the direct uniform attack of the Al matrix including the hardening particles corresponds to the first breakdown potential.

The TEM micrographs in Fig. 3 show the AA7xxx-T6 micro-structure, where fine

hardening precipitates of less than 1 nm in size are in the matrix, and relatively coarse precipitates of about 50 nm and PFZ are on the grain boundary. The area or volume fraction of
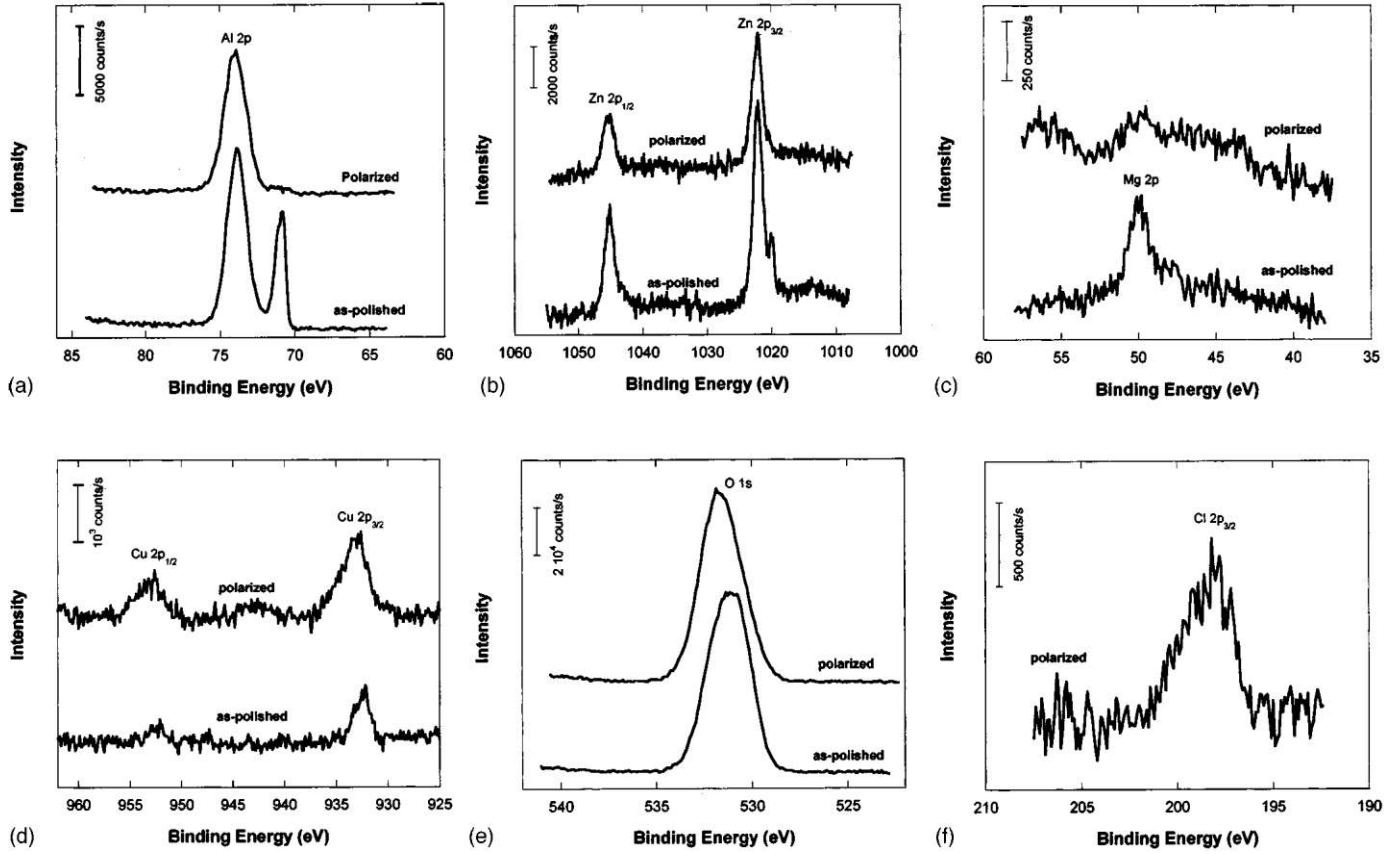

Figure 13. XPS spectra measured from samples of AA7075 after mechanical polishing and a subsequent polarization at —725 mV$_{SCE}$ for 500 s in deaerated 0.5 M NaCl at pH 3.56; (a) Al 2p, (b) Zn 2p, (c) Mg 2p, (d) Cu 2p, (e) O 1s, and Cl 2p.

Table IV. Data obtained from XPS spectra.

| Element	Compound	State	BE (eV)	FWHM[a] (eV)	Sample
Al 2p	Al in matrix	Al^0	70.95	0.81	Polished
Al 2p	γ-Al$_2$O$_3$/Al(OH)$_3$	Al^{3+}	73.83	1.56	Polished
Al 2p	Al(OH)$_3$	Al^{3+}	74.06	1.78	Polarized
Zn 2p3/2	Zn in matrix	Zn^0	1022.10	1.88	Polished
Zn 2p3/2	Zn in Al(OH)$_3$	Zn^0	1022.10	1.84	Polarized
Mg 2p	Mg in matrix	Mg^0	49.94	1.69	Polished
Mg 2p	...	...	...	...	Polarized
Cu 2p3/2	Cu in matrix	Cu^0	932.31	1.6	Polished
Cu 2p3/2	Cu in Al(OH)$_3$	Cu^0	932.83	2.77	Polarized
O 1s	γ-Al$_2$O$_3$/Al(OH)$_3$	O^{2-}/OH$^-$	531.06	2.65	Polished
O 1s	Al(OH)$_3$	OH$^-$	531.68	2.55	Polarized
Cl 2p3/2	Chloride	Cl$^-$	198.21	2.68	Polarized

[a] Full width at half-maximum.
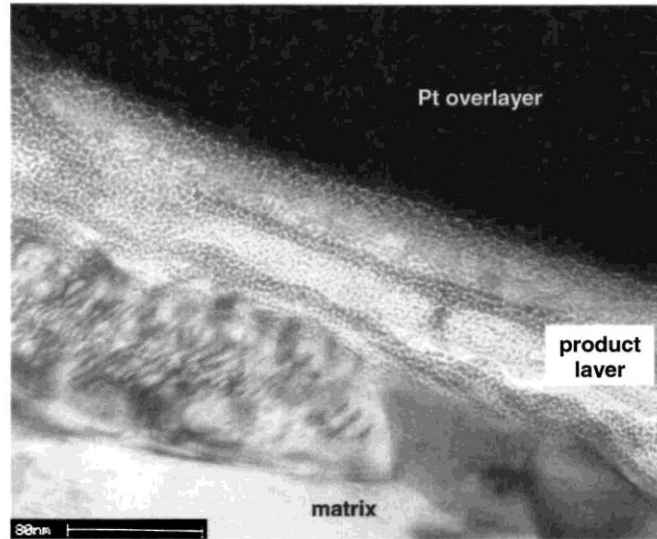
Figure 14. TEM micrograph of the product layer formed on AA7075-T6 when polarized at —725 mV$_{SCE}$ for 500 s in deaerated 0.5 M NaCl at pH 3.56.

fine hardening precipitates is much greater than that of grain boundary precipitates. It is impossible to determine the composition of the hardening particles directly because of their very small size. According to physical metallurgy of Al alloys, fine hardening precipitates and grain boundary precipitates should have similar composition in the T6 temper. In this work, the compositions of grain boundary precipitates were determined using STEM/Nano-EDS. Figure 4 reveals that Cu content in grain boundary Mg(ZnAlCu)$_2$ phase precipitates dramatically increased and Zn decreased with alloy Cu content. This variation of composition is probably also true for the fine hardening precipitates (GP zones and η′), which have similar composition to the grain boundary precipitates. Ramgopal *et al.* deposited thin-film analogs of Mg(ZnCuAl)$_2$ precipitates and investigated their electrochemical behavior in deaerated 0.5 M NaCl. They found that breakdown potential of Mg(ZnCuAl)$_2$ analogs increased with Cu content.[13] The breakdown of these thin-film analogs appeared to be a localized dealloying phenomenon. The breakdown potentials they measured were lower than the first breakdown potentials of the alloys studied in this investigation. Also, they found that a considerable amount of Cu (17 atom %) was needed to increase the breakdown potential beyond that of MgZn$_2$. Despite these differences, the trend of increasing breakdown potential of Mg(ZnCuAl)$_2$ with increasing Cu content is useful for explaining the behavior of the alloys studied in this investigation.

The Cu content of the Mg(ZnCuAl)$_2$ grain boundary precipitates and fine hardening precipitates in the matrix increases with increasing alloy Cu content. The breakdown potential associated with dealloying for Mg(ZnCuAl)$_2$ analogs was shown to increase with Cu content. These observations can be combined to explain the increasing trend of E_1 with alloy Cu content by considering that the first breakdown potential in Cu-containing AA7xxx-T6 is the result of preferential dissolution or dealloying of fine Mg(ZnCuAl)$_2$ hardening precipitates in the matrix. Since these fine hardening precipitates are highly dispersed coherently or semicoherently in the Al solid solution containing Zn, Mg, and Cu, the preferential dissolution of these fine precipitates may also cause the reaction of the Al solid solution in the matrix. This combined dissolution of fine hardening precipitates and surrounding Al solid solution results in the

formation of an Al(OH)$_3$ product layer, which limits the depth of attack, making it a transient process. Attack of the grain boundary particles is also possible, but IGC does not develop until longer hold times or higher potentials for kinetic reasons, as discussed below.
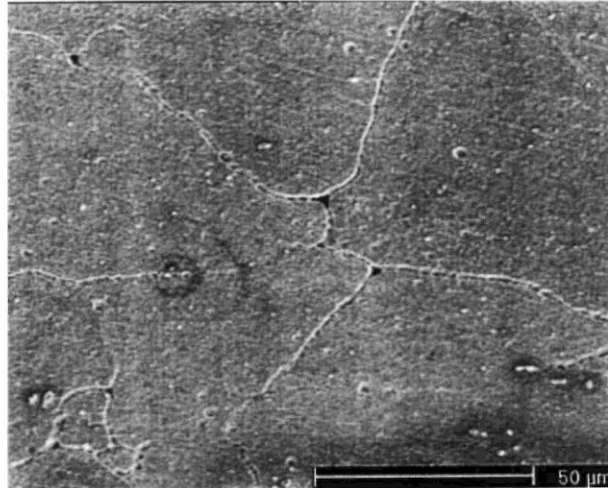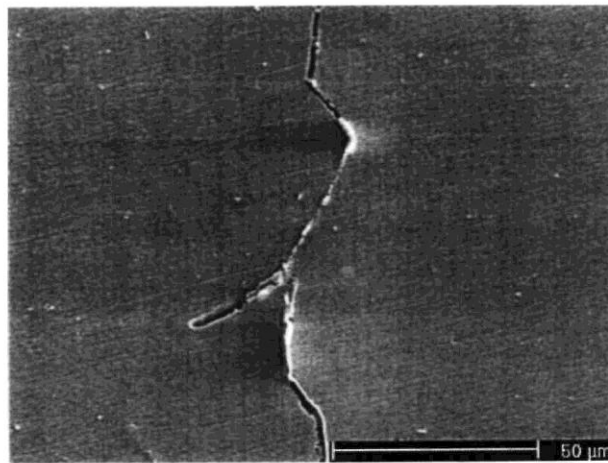
Figure 15. SEM micrographs of the surface of (a) AA7039-T6 polarized at — 870 mV$_{SCE}$, and (b) AA7050-T6 polarized at —720 mV$_{SCE}$ in deaerated 0.5 M NaCl at pH 3.56 for 24 h.

When the applied potential is above the second breakdown potential (E_2), stable pits from on the matrix by breakdown of the passive film or Al(OH)$_3$ formed between E_1 and E_2. The breakdown potential for stable pitting or dissolution is dependent upon the composition of 7xxx alloys, which are composed of mainly Al and a small amount of alloying elements including 4-6 wt % Zn, 1.6-3 wt % Mg, and 0-2 wt % Cu. Muller and Galvele have systematically investigated the pitting potential of high purity binary Al-Zn, Al-Mg, and Al-Cu solid solutions.[27,28] Zn, Mg, and Cu as solute elements in binary solid solution Al alloys had different effects on the pitting potential. The pitting potential decreased greatly with increasing Zn content up to 3 wt % and

then remained constant with further increase in Zn content. There was no influence of Mg on pitting potential. Pitting potential increased dramatically with increasing Cu content up to 5 wt %. In this study, the STEM/Nano-EDS composition measurements revealed that the composition of the Al matrix including the fine hardening particles was very close to the alloy composition. Above E_2, selected grain attack or matrix dissolution is evident in the corrosion morphology as well as IGC. The pits are much larger than the size of the fine hardening particles, so it is reasonable to consider the matrix with hardening particles to be a homogeneous phase regarding pit stability. Therefore, the increase in the second breakdown potential corresponding to stable
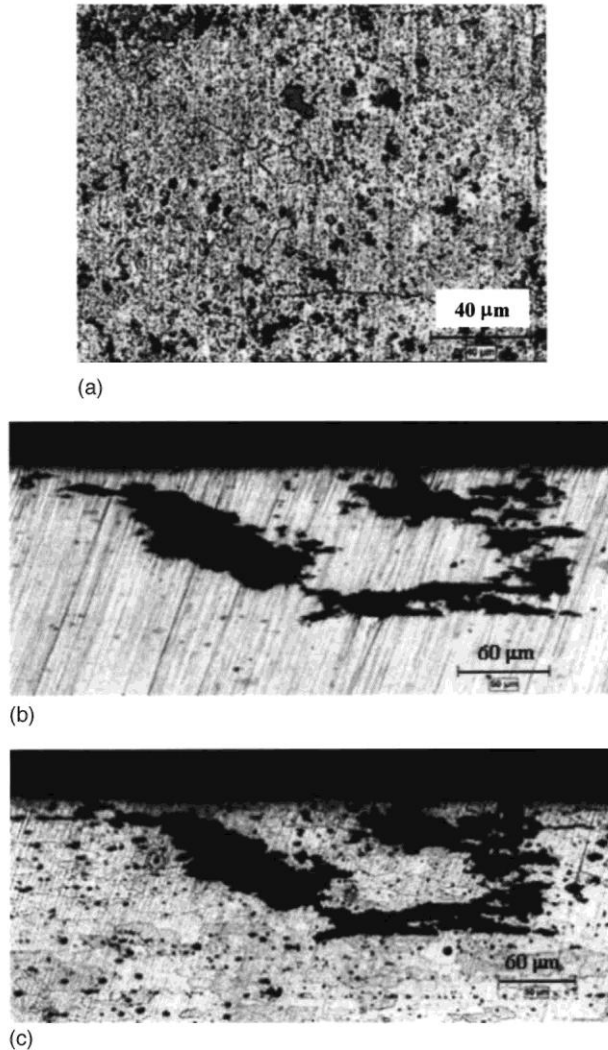

Figure 16. Metallographical micrograph of (a) top surface, (b) as polished cross section, and (c) etched cross section of AA7075-T6 polarized in deaerated 0.5 M NaCl at pH 3.56 at —680 mV$_{SCE}$ for 5 h.

dissolution in AA7xxx-T6 with increasing alloy Cu content can be explained by the increase in Cu content in the Al. As shown in Table I, Zn content also increased with increasing Cu content in the Cu-containing alloys. Therefore, ignoring the effect of Cu, the data in Fig. 6 indicate that

the breakdown potentials in the Cu-containing alloys actually increase with increasing Zn content, which is opposite to the effect of Zn in binary alloys. This proves that the influence of Cu is dominant. The decrease in E_2 from 7039 (0.077 wt % Cu, 4.0 wt % Zn) to 7004 (0.013 wt % Cu, 4.3 wt % Zn) may result from both the lower Cu content and the slightly higher Zn content.

Another interesting phenomenon is that shallow IGC formed and propagated on the surface during long-term polarization between E_1 and E_2 (Fig. 15), or deeply into the alloys above E_2 along with selective grain attack (Fig. 16 and 17). The more-severe attack observed for the higher Cu alloy at a controlled potential between E_1 and E_2 in deaerated solution is in contradiction to the observation of increasing breakdown potential with increasing Cu content. Furthermore, it is not consistent with the viewpoint of Ramgopal *et al*, who indicated that higher dissolved Cu concentration in intergranular crevices in T7 temper alloys decreases the severity of attack relative to the T6 temper. It is worthwhile mentioning the effect of temper on the polarization behavior. Only one breakdown potential was found for AA7075-T7 orAA7150-T7 in deaerated chloride solution. The single breakdown potential for either of the alloys in the T7 temper was equal to the first breakdown potential for the T6 temper. It is possible that the T7 temper decreases the critical current density for stable pitting, and thus decreases the breakdown potential for stable dissolution or pitting.
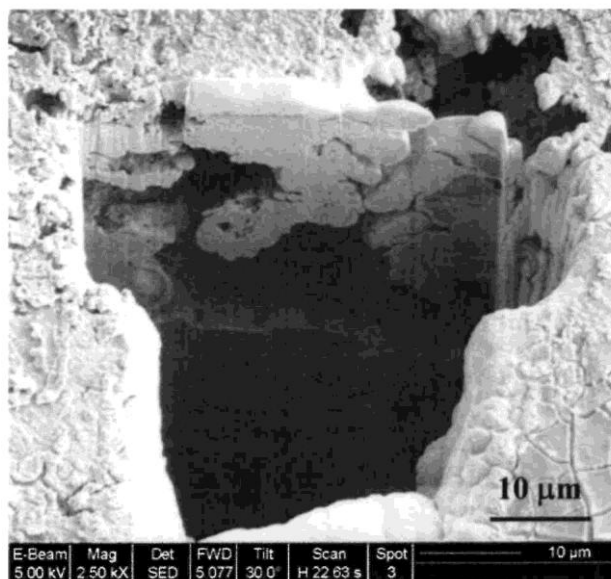

Figure 17. SEM micrograph of FIB cross section of the same AA7075 sample as in Fig. 16 polarized at —680 mV$_{SCE}$ in deaerated 0.5 M NaCl at pH 3.56 for 5 h, evidencing microstructural pitting.

Role of Cu content in corrosion resistance of AA7xxx-T6.—Electrochemical studies in this work reveal that corrosion behavior of AA7xxx-T6 is strongly dependent on Cu content. The breakdown potentials measured in deaerated chloride solution increase with alloy Cu content. The second breakdown potentials are more important than the first breakdown potentials because the second breakdown potential corresponds to the stable dissolution or localized corrosion, while the first breakdown potential corresponds to transient dissolution. From this viewpoint,

increasing Cu content is beneficial to the localized corrosion resistance of AA7xxx because of its effect on increasing the breakdown potentials. The increase in breakdown potential with Cu content may be related to the beneficial role of Cu in increasing resistance of AA7xxx to stress corrosion cracking.[4] However, the corrosion resistance of the alloys at open circuit in aerated
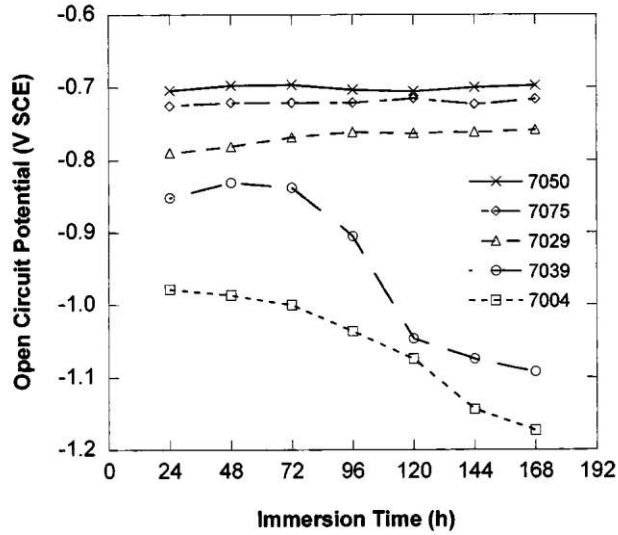

Figure 18. Time evolution of the OCPs of AA7xxx-T6 within 168 h immersion in aerated 0.5 M NaCl.
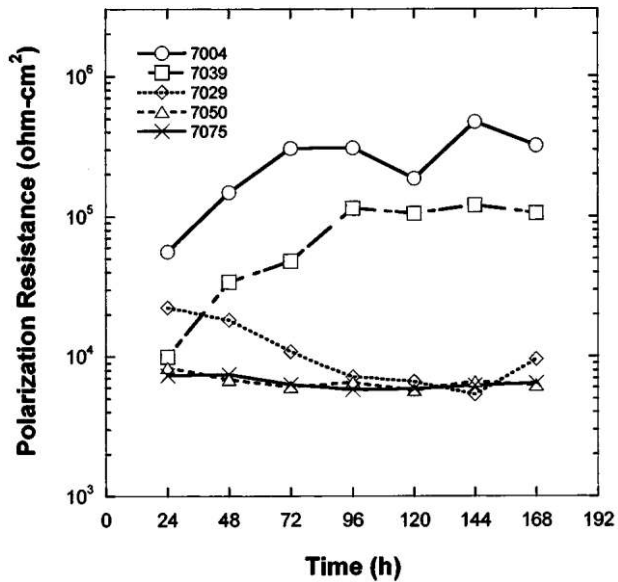

Figure 19. Polarization resistance determined by EIS tests as a function of immersion time for AA7xxx-T6 in aerated 0.5 M NaCl.

solution decreases with increasing alloy Cu content. These contradictory effects of Cu content must be rationalized.

One important consideration is the role of Cu on the OCP. Figure 18 presents the evolution of the OCP in aerated solutions over a period of 1 week. The OCP evolution in the deaerated solution during a shorter period, the stabilization period prior to potentiodynamic polarization tests, is given in Fig. 20. The relationship between the breakdown potentials and the OCPs in deaerated and aerated chloride solutions is given in Fig. 21. This figure combines the data of Fig. 6, 18, and 20. The OCPs in deaerated solution after about 30 min prior to the polarization tests are denoted by triangles. The range of OCP in deaerated solution during this period is given by the solid double-ended arrows. The OCPs in aerated solution after 168 h are denoted by crosses and are connected by a line. The range of OCP in aerated solution during this period is given by the dashed double-ended arrows. The variations in potential for AA7075 and AA7050 in aerated solution were so small that they were not included. In deaerated solution, the OCPs for all alloys except Cu-free AA7004 were below their respective first breakdown potentials. The OCP for AA7004 in deaerated solution was —960 mV$_{SCE}$ within about the first 250 s. This is just below its breakdown potential (—951 mV$_{SCE}$). Then the OCP decreased with the immersion time until a stable value, —1040 mV$_/$, was reached. We may assume that the single breakdown potential for AA7004 is its second breakdown potential and its first breakdown potential is given by the extrapolation of line of the E_1 values from the other alloys, about —985 mV$_{SCE}$. The exposure of AA7004 during the open-circuit stabilization period at potentials above its E_1 would have resulted in dissolution of the Cu-free η precipitates similar to the behavior of the Cu-containing alloys during potentiostatic exposure to potentials between their E_1 and E_2 values. As a result, the transient dissolution associated with E_1 was not observed on the subsequent polarization scan and only stable localized corrosion associated with E_2 was observed. This is similar to the behavior of AA7075-T6 during repeated cyclic polarization shown in Fig. 10.
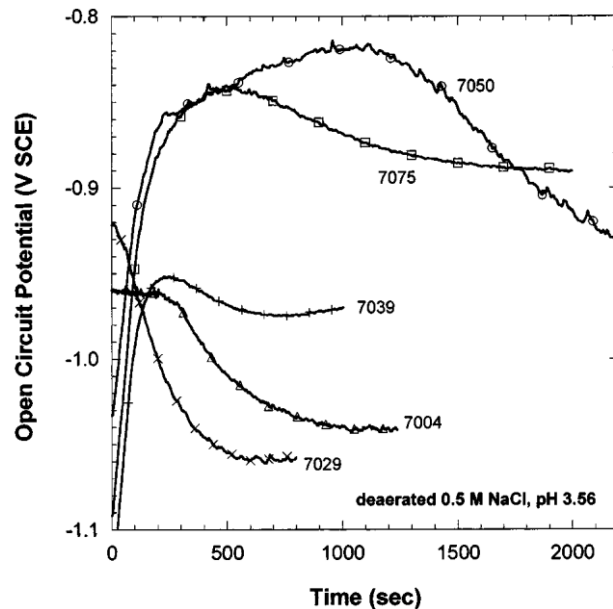

Figure 20. OCP *vs.* time for 7xxx-T6 in deaerated 0.5 M NaCl at pH 3.56.
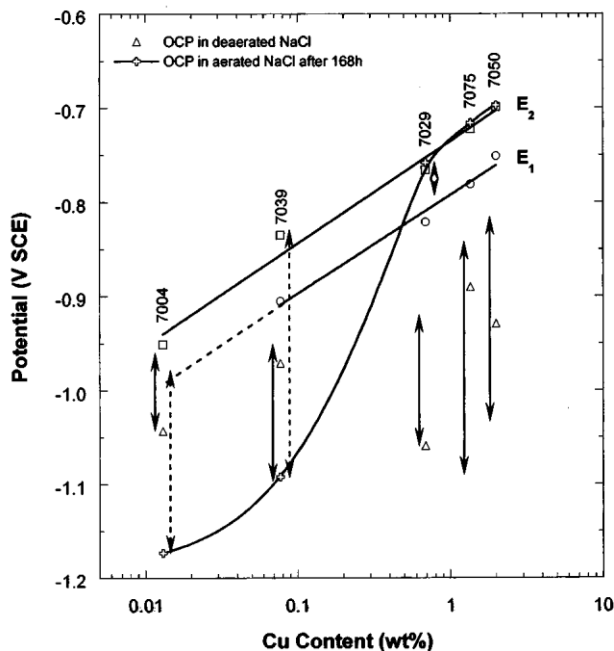
Figure 21. Comparison of the breakdown potentials and the OCPs in deaerated and aerated chloride solutions. E_1 and E_2 are denoted by circles and squares, respectively. The OCPs in deaerated solution at pH 3.56 after about 30 min prior to the polarization tests are denoted by triangles. The range of OCP in deaerated solution during this period is given by the solid double-ended arrows. The OCPs in aerated solution after 168 h are denoted by crosses and are connected by a line. The range of OCP in aerated solution during this period is given by the dashed double-ended arrows. The variations in potential for AA7075 and AA7050 in aerated solution were so small that they were not included.

Experiments were performed in an attempt to evaluate this possibility by avoiding open-circuit exposure at higher potentials. An AA7004 sample was immersed into deaerated 0.5 M NaCl at pH 3.56 under potential control at —1.15 V_{SCE}. To prevent possible overload of the potentiostat during immersion, an AA7039 sample was polarized at —1.15 V_{SCE} prior to immersion of the AA7004 sample. The AA7004 sample was electrically shorted to the AA7039 sample, immersed in the solution, and then the AA7039 sample was disconnected electrically. The subsequent experiment was performed only on the AA7004 sample. The Gamry Virtual Front Panel (VFP)software was used in this experiment to avoid any open-circuit exposure. After 2 min polarization at —1.15 V_{SCE}, the potential was scanned upward at a rate of 0.2 mV/s. In this fashion, the potentiodynamic polarization curve for AA7004 was obtained as shown in Fig. 22b. Only one breakdown potential was found again and its value was the same as found previously. This sample was not exposed at a higher OCP, and the absence of a breakdown at the expected E_1 value suggests that AA7004 does not exhibit the phenomenon associated with the first breakdown potential.

      Another AA7004 sample was immersed for 2 min under potential control at —1.15 V_{SCE} in the same fashion, and then jumped to —930 mV_{SCE} and held there for 1 h, Fig. 23. Figure 23 also shows the result for a sample held at —930 mV_{SCE} after OCP exposure for 30 min in deaerated chloride solution, as was the procedure for all experiments shown in Fig. 7 and 8. A large current transient was found during the first 400 s for the sample that was not first exposed at open circuit. After the transient, the current density was nearly the same as the value for the

AA7004 sample that was first exposed at OCP for 30 min. This result contradicts the previous result and suggests that Cu-free AA7004 does exhibit the transient dissolution phenomenon associated with E_1.

Further work is required to resolve the contradictory data regarding AA7004. It is possible that the transient dissolution phenomenon occurs, but is difficult to observe at low potentials in AA7004. It is also possible that the transient dissolution phenomenon does not occur because some Cu content is needed. Dealloying of Mg and Zn from the η phase precipitates may occur at extremely low potentials and therefore be difficult to sense electrochemically.[17] In a Cu-containing alloy, the η phase precipitates would contain some amount of Cu and dealloying would leave a Cu-rich remnant. In this view, E_1 may be associated with the breakdown of this Cu-rich remnant layer. In a Cu-free alloy, this layer would not be present, and η phase precipitates would just suffer the very low potential attack. At higher potentials, all alloys exhibit the matrix breakdown and IGC associated with E_2.
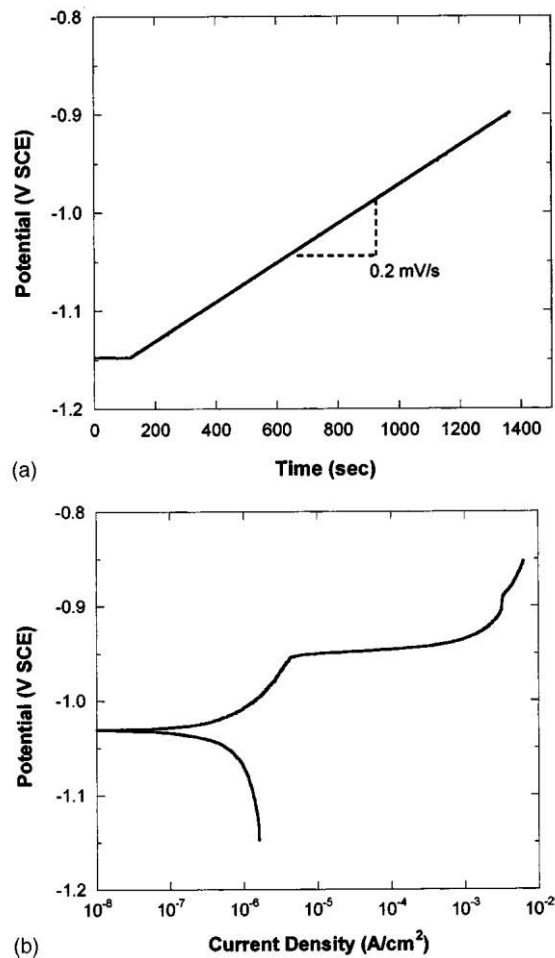

Figure 22. (a) Time evolution of the potential applied to AA7004-T6 and (b) potentiodynamic polarization curve for AA7004-T6 after 2 min holding at — 1.15 V_{SCE} showing only one breakdown potential for AA7004-T6. The solution was deaerated 0.5 M NaCl at pH 3.56 and the scan rate was 0.2 mV/s.
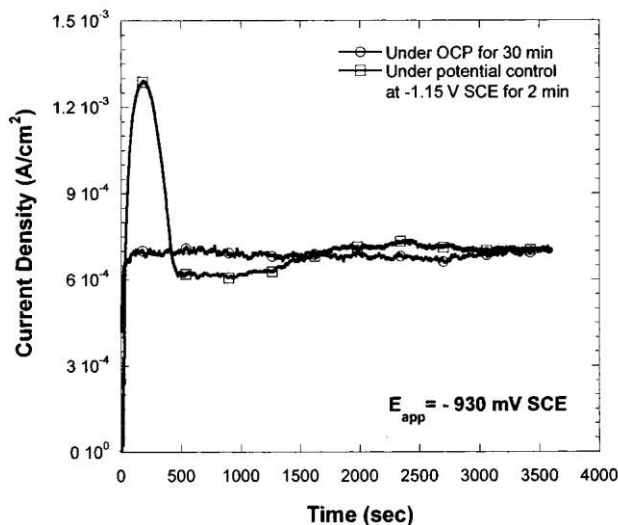
Figure 23. Potentiostatic polarization curve for AA7004-T6 at —930 mV$_{SCE}$ for 1 h in deaerated 0.5 M NaCl at pH 3.56 under two different conditions before polarization: (a) under OCP for 30 min and (b) under potential control at —1150 mV$_{SCE}$ for 2 min.

As described above, the breakdown potentials measured in deaerated solutions increased with increasing alloy Cu content, but the corrosion resistance measured at open circuit in aerated solutions decreased with increasing Cu content. The contradictory behavior in deaerated and aerated solutions can be understood by considering the OCP in aerated solution. As shown in Fig. 19 and 21, the OCPs during 1 week in aerated solution are quite different for the different alloys. For Cu-free AA7004, the OCP started out just above its E_1, but then dropped down to very low values after several days. The OCP for AA7039, with extremely low Cu content, reached a value approximately equal to its E_2 after 2 days and then also decreased with immersion time to very low values. From the comparison of OCP and breakdown potentials for these alloys, it is expected that the transient dissolution associated with the fine hardening particles would occur during the early stages of exposure. Some IGC or selective grain attack could have taken place in AA7039 during the period when its OCP of was close to its E_2. However, the long-term behavior indicates that sustained localized attack was not possible. This is supported by the high polarization resistances measured during the exposure to the aerated solution. In sharp contrast, the OCPs for other three alloys with intermediate and high Cu content remained at high values, which are a little higher than their own second breakdown potentials. As mentioned above, this is likely the result of Cu enrichment at the surface, which enhances the oxygen reduction reaction in aerated solutions. The potential is pinned close to the breakdown potential associated with stable attack (E_2) because of the relative non-polarizability of the localized corrosion reactions. Sustained localized corrosion is possible at these potentials, as is reflected by the decrease in polarization resistance with increasing Cu content. Hence, the overall effect of Cu content is detrimental to localized corrosion resistance of AA7xxx in aerated solutions.

Conclusions

In this study, the corrosion behavior of 7xxx alloys in the T6 temper with various Cu

contents was investigated using a combination of SEM, TEM, STEM, and XPS analysis of the microstructure. The following conclusions are drawn

1. Two breakdown potentials were observed for all alloys except for essentially Cu-free AA7004. The two breakdown potentials increase logarithmically with alloy Cu content in deaerated chloride solution.

2. The first breakdown potential corresponds to transient dissolution associated with attack of the fine hardening particles and the surrounding solid solution in a thin surface layer. The Cu content of these particles likely mirrors that of the grain boundary particles, which increase in Cu content as the alloy Cu content increases. The Cu content in the hardening particles controls the first breakdown potential.

3. The second breakdown potential is associated with combined IGC and selective grain attack, and is controlled by the Cu content in the matrix, including the hardening particles.

4. IGC develops after long times at potentials between the two breakdown potentials.

5. Under free corrosion conditions in aerated chloride solutions, the corrosion potential increases and the polarization resistance decreases as the Cu content increases as a result of Cu enrichment on the surface, which facilitates the oxygen reduction reaction. Because of this effect, the overall influence of Cu on the corrosion behavior is detrimental, despite the increase in breakdown potentials with Cu content.

Acknowledgments

References

1. R. G. Buchheit, M. A. Martinez, and L. P. Montes, *J. Electrochem. Soc.*, **147**, 119 (2000).
2. R. G. Buchheit and R. K. Boger, in *Localized Corrosion Proceedings of the Research Topical Symposium*, NACE, Houston, TX, p. 265 (2001).
3. N. Dimitrov, J. A. Mann, M. Vukirovic, and K. Sieradzki, *J. Electrochem. Soc.*, **147**, 3283 (2000).
4. J. E. Hatch, *Aluminum: Properties and Physical Metallurgy*, ASM, Metals Park, OH (1983).
5. R. P. Wei, C.-M. Liao, and M. Gao, *Metall. Mater. Trans. A*, **29**, 1153 (1998).
6. M. Gao, C. R. Feng, and R. P. Wei, *Metall. Mater. Trans. A,* **29**, 1145 (1998).
7. M. Puiggali, A. Zielinski, J. M. Olive, E. Renauld, D. Desjardins, and M. Cid, *Corros. Sci.*, **40**, 805 (1998).
8. E. Lunarska, E. Trela, and Z. Szklarska-Smialowska, *Corrosion (Houston)*, **43**, 219 (1987).
9. T. Ramgopal, P. I. Gouma, and G. S. Frankel, *Corrosion (Houston),* **58**, 687 (2002).
10. J. K. Park and A. J. Ardell, *Metall. Mater. Trans. A*, **15**, 1531 (1984).
11. J. K. Park and A. J. Ardell, *Acta Metall. Mater*, **39**, 591 (1991).
12. S. Maitra and G. C. English, *Metall. Mater. Trans. A*, **12**, 535 (1981).
13. T. Ramgopal, P. Schmutz, and G. S. Frankel, *J. Electrochem. Soc.*, **148**, B348 (2001).
14. R. G. Buchheit, J. P. Moran, and G. E. Stoner, *Corrosion (Houston)*, **46**, 610 (1990).
15. R. G. Buchheit, J. P. Moran, and G. E. Stoner, *Corrosion (Houston)*, **50**, 120 (1994).
16. R. G. Buchheit, F D. Wall, G. E. Stoner, and J. P. Moran, *Corrosion (Houston)*, **51**, 417 (1995).
17. D. B. Williams and C. B. Carter, *Transmission Electron Microscopy: A Textbook for Materials Science*, Plenum Press, New York (1996).
18. D. D. Macdonald and M. Urquidi-Macdonald, *J. Electrochem. Soc.*, **132**, 2316 (1985).
19. J. F Moulder, W. F Stickle, P. E. Sobol, and K. D. Bomben, *Handbook of X-Ray Photoelectron Spectroscopy*, Perkin-Elmer Corporation, Eden Prairie, MN (1992).

20. *Annual Book of ASTM Standards*, Vol. 03.02, p. 163, ASTM, Philadelphia, PA (1995).

21. R. G. Buchheit, R. P. Grant, P. F Hlava, B. Mckenzie, and G. L. Zender, *J. Electrochem. Soc*., **144**, 2621 (1997).

22. R. G. Buchheit, R. K. Boger, M. C. Carroll, R. M. Leard, C. Paglia, and J. L. Searles, *JOM*, **53**, 29 (2001).

23. N. Dimtrov, J. A. Mann, and K. Sieradzki, *J. Electrochem. Soc.*, **146**, 98 (1999).

24. M. B. Vukmirovic, N. Dimitrov, and K. Sieradzki, *J. Electrochem. Soc.*, **149**, B428 (2002).

25. H. M. Obispo, L. E. Murr, R. M. Arrowood, and E. A. Trillo, *J. Mater. Sci*., **35**, 3479 (2000).

26. R. G. Buchheit, L. P. Montes, M. A. Martinez, J. Micheal, and P. F Hlava, *J. Electrochem. Soc*., **146**, 4424 (1999).

27. I. L. Muller and J. R. Galvele, *Corros. Sci*., **17**, 995 (1977).

28. I. L. Muller and J. R. Galvele, *Corros. Sci*., **17**, 179 (1977).